Epigenetic modulation in the pathogenesis and treatment of inherited aortic aneurysm conditions

Authors: Benjamin E. Kang[1], Rustam Bagirzadeh[1], Djahida Bedja[1], Jefferson J. Doyle[1], Elena G. MacFarlane[1], Harry C. Dietz[1,2]*

Affiliations:

[1]Department of Genetic Medicine, Johns Hopkins University School of Medicine, Baltimore, MD 21205, USA.

[2]Howard Hughes Medical Institute, Chevy Chase, MD 20815, USA.

* To whom correspondence should be addressed:

Hal C. Dietz

Professor, Institute of Genetic Medicine

Investigator, Howard Hughes Medical Institute

Johns Hopkins University School of Medicine

Miller Research Building Room 539

733 N. Broadway

Baltimore, MD. 21205

hdietz@jhmi.edu

410-614-0701

Competing interests: B.E.K. and H.C.D are inventors on a patent application entitled "Targeted Epigenetic Therapy For Inherited Aortic Aneurysm Condition," (no. PCT/US2018/49217), jointly filed on 31st August 2018 by the Johns Hopkins University School of Medicine. All other authors declare that they have no competing interests.

Abstract

Shprintzen-Goldberg syndrome (SGS) is a rare systemic connective tissue disorder characterized by craniofacial, skeletal, neurodevelopmental, cutaneous, and cardiovascular manifestations, including aortic root aneurysm. It has significant phenotypic overlap with both Marfan syndrome (MFS) and Loeys-Dietz syndrome (LDS). We previously reported that SGS is caused by heterozygous mutations in the Sloan-Kettering Institute proto-oncogene (*SKI*), which encodes a potent suppressor of transforming growth factor beta (TGFβ) target gene expression. Herein, we show that mouse lines harboring orthologous amino acid substitutions in *Ski* recapitulate multiple human SGS phenotypic manifestations, including skin collagen deposition, skeletal kyphosis, behavioral hypoactivity, and aortic root aneurysm. Furthermore, aortic root aneurysm in SGS mice is associated with both increased acetylation of histone H3 at lysine-27 (H3K27) and TGFβ target gene expression, all of which can be ameliorated by pharmacological CBP/P300 inhibition in vivo; similar findings were seen in cultured dermal fibroblast from SGS patients. Aortic root growth is also abrogated in a mouse model of MFS by selective CBP/P300 inhibition in association with blunted expression of TGFβ target genes. These data document excessive H3K27 acetylation and hence TGFβ target gene expression in the pathogenesis of inherited presentations of aortic root aneurysm and the therapeutic potential of pharmacological epigenetic modulation.

Introduction

Shprintzen-Goldberg syndrome (SGS) is a rare, autosomal dominant systemic connective tissue disorder (CTD) characterized by craniosynostosis, severe skeletal deformities, aortic root dilatation, minimal subcutaneous fat, intellectual disability, and neurodevelopmental anomalies (1, 2). It shows considerable phenotypic overlap in the craniofacial, skeletal, skin and cardiovascular systems with both Marfan syndrome (MFS) and Loeys-Dietz syndrome (LDS), with the additional findings of mental retardation and severe skeletal muscle hypotonia.

Mutations in the *FBN1* gene encoding the extracellular matrix protein fibrillin-1 cause MFS, while heterozygous mutations in the genes encoding TGFβ ligands (*TGFB2* or *TGFB3*), receptor subunits (*TGFBR1* or *TGFBR2*) or intracellular signaling intermediates (*SMAD2* or *SMAD3*) cause LDS (3, 4). This has led to the recognition that dysregulated TGFβ signaling plays a role in the pathogenesis of both MFS and LDS (4, 5). In prior work, we have demonstrated increased activation of both canonical (i.e. Smad2/3) and non-Smad (i.e. MAPK; Erk1/2) TGFβ-dependent signaling cascades in affected tissues of MFS and LDS mouse models (5-8). Furthermore, multiple phenotypic manifestations in mice, including aortic root aneurysm, can be ameliorated by postnatal administration of TGFβ-neutralizing antibody, and/or the angiotensin II (Ang-II) type 1 (AT1) receptor blocker (ARB) losartan, in association with blunted Smad2/3 and Erk1/2 activation (7, 9-11). We also demonstrated that genetic ablation of *Smad2* in cardiac neural crest-derived vascular smooth muscle cells could abrogate aortic root aneurysm formation in mice with LDS caused by a kinase domain mutation in *Tgfbr1* (12). This occurred in association with normalization of the tissue signature for excessive TGFβ signaling in the aortic wall.

Despite these observations, there were a number of controversies that derived from this initial work. First, certain features of SGS, including craniosynostosis, altered palatogenesis, and

68   aortic aneurysm, have variably been associated with low TGFβ signaling states (13-15). This

69   raised the question as to whether low or high TGFβ signaling drives disease pathogenesis in SGS

70   and related CTDs. This has been further brought into question by the observation that LDS is

71   predominantly caused by heterozygous missense substitutions affecting the kinase domain of

72   either TGFβR1 or TGFβR2, that can cause a context-specific decline in TGFβ signal propagation

73   in cell culture systems (4, 16). Furthermore, LDS-like phenotypes are caused by heterozygous

74   loss-of-function mutations in *SMAD3,TGFB2*, or *TGFB3*, all positive effectors of TGFβ signaling

75   (17, 18). Once again, haploinsufficiency for these genes associated with a tissue signature for high

76   TGFβ signaling including excessive phosphorylation and nuclear translocation of Smad2/3 and

77   enhanced expression of typical TGFβ target genes including *COL1A1*, *COL3A1*, *CTGF*, *MMP2*

78   and *MMP9* (17, 19, 20). Taken together, these seemingly contradictory data have engendered

79   considerable controversy regarding the precise role of TGFβ signaling in the pathogenesis of

80   inherited forms of thoracic aortic aneurysm.

81   Given the extensive phenotypic overlap of SGS with both MFS and LDS, we hypothesized

82   that aberrant TGFβ activation likely underlies SGS and that identification of the genetic basis of

83   the syndrome would likely inform our understanding of both it and related CTDs. We and others

84   previously identified that de novo heterozygous mutations in the receptor-activated SMAD (R-

85   SMAD) binding domain of the Sloan-Kettering Institute proto-oncogene (*SKI*), a known repressor

86   of TGFβ signaling, cause SGS (21, 22). Furthermore, primary dermal fibroblasts from SGS

87   patients grown at steady-state showed a cell-autonomous increase in transcriptional output of many

88   TGFβ–responsive genes. These data supported the conclusion that SGS pathogenesis appears to

89   be driven by high TGFβ signaling, presumably from loss of suppression by mutant SKI protein. It

4

90   remains unclear, however, whether these mutations in *SKI* drive SGS pathogenesis via a loss-of-

91   function, dominant-negative, or gain-of-function mechanism.

92   Because of the plethora of SKI binding partners, the downstream consequences of *SKI*

93   mutations remain uncertain. SKI appears to bind to an array of partners, including R-SMADs

94   (SMAD2 and SMAD3), SMAD4, SKI itself (during dimerization), as well as SKI-like peptide

95   (SKIL), and transcription factors such as CBP/P300, mSin3A, SNW1, N-CoR and HDAC1 (23-

96   30). SGS-causing mutations have to date clustered in the R-SMAD binding domain of SKI towards

97   the N-terminal end of the protein, including substitution of an amino acid that has previously been

98   shown to be essential for SKI-SMAD3 interactions (e.g. p.Leu21Arg) (30). Interestingly, a version

99   of SKI lacking this R-SMAD binding domain retained its ability to regulate SMAD-mediated

100   transcriptional activation in a transient transfection-based reporter system, but failed to dissociate

101   CBP/P300 from the SMAD complex (28, 30), suggesting that CBP/P300 could play a role in SGS.

102   More recently, it was shown that regulated degradation of SKI requires interaction with SMAD2

103   or SMAD3 and SMAD4; SGS mutations that prevent SMAD2/3 binding resulted in increased

104   stability and hence abundance of mutant SKI, which retained the ability for transcriptional

105   repression of some TGFβ target genes, as evidenced by reduced induction of these transcripts in

106   cultured cells expressing mutant SKI to acute stimulation with exogenous TGFβ (31). Many

107   questions remain regarding the potentially opposing influences of different aspects of altered SKI

108   homeostasis in SGS including increased stability and abundance that is perhaps offset by altered

109   efficiency for recruitment to regulatory elements of target genes. Given that SGS-causing

110   mutations in SKI protein interfere with binding to pSMAD2 and pSMAD3, altered transcriptional

111   regulation is presumably mediated through interaction with SMAD4 only and by aberrant

112   regulation of epigenetic modulators such as CBP/P300. The net effect of heterozygous SGS

113   mutations on TGFβ signaling may vary based on cell type, baseline signaling status, redundancy

114   of autoregulatory factors, and the potential for chronic compensatory events.

115   In an attempt to inform these questions, we generated and characterized a knock-in mouse

116   model of SGS and explored the molecular mechanisms driving disease pathogenesis in these

117   animals. We used this information to develop a novel therapeutic strategy for the disorder, which

118   also shows efficacy in a well-characterized mouse model of MFS. Finally, we show concordant

119   molecular events and therapeutic potential in cultured dermal fibroblasts from patients with SGS.

120

121   **Results**

122   *SGS mouse models recapitulate the phenotype of patients with SGS*

123   To determine whether mutations in SKI are sufficient to recapitulate the SGS phenotype in

124   mice, several targeted mouse lines were developed (Fig. 1A). $Ski^{+/-}$ mice are heterozygous for a

125   deletion of exons 2 and 3 of *Ski,* which leads to functional haploinsufficiency due to nonsense-

126   mediated mRNA decay. $Ski^{G34D/+:Neo}$ mice are heterozygous for a missense mutation (p.Gly34Asp)

127   previously observed in a patient with severe SGS (21); this allele retains the neomycin resistance

128   cassette, which causes transcriptional interference and also leads to functional haploinsufficiency.

129    $Ski^{G34D/+}$ mice are generated by breeding of $Ski^{G34D/+:Neo}$ mice to transgenic mice expressing an

130   ubiquitous Cre recombinase (CMV-Cre), which eliminates the Neo cassette, thus allowing

131   transcription of the mutant allele and expression of mutant SKI. As expected, both

132   haploinsufficient lines expressed half the normal complement of *Ski* mRNA, while the

133   heterozygous $Ski^{G34D/+}$ line expressed significantly higher levels of *Ski* mRNA, to levels

134   indistinguishable from control mice (Fig. 1B). The $Ski^{G34D/+}$ mouse line uniquely expressed the

135   mutant allele, as shown by a diagnostic BamH1 restriction fragment of amplified cDNA that was

136   present only in this line (Fig. 1C).

137   Mice heterozygous for the mutant allele ($Ski^{G34D/+}$) recapitulated multiple phenotypic

138   characteristics of patients with SGS. In vivo echocardiography of these mice showed evidence of

139   increased aortic root size at 6 months of age and enhanced post-natal aortic root growth from 2 to

140   6 months of age, compared to wild-type (WT) littermates (Fig. 1D, S1A). They also showed

141   evidence of skeletal deformity in the form of spine kyphosis (Fig. 1F), as well as reduced

142   subcutaneous fat and increased collagen deposition in the skin (Fig. S1B, C), at 6 months of age,

143   in comparison to WT littermates. Finally, they displayed abnormal behavior including hypoactivity

144   and impaired motor performance at 10 weeks of age, when compared to WT littermates (Fig. S1D,

145   E). In contrast, mice haploinsufficient for Ski ($Ski^{+/-}$ or $Ski^{G34D/+:Neo}$) showed no evidence of these

146   phenotypic defects when compared to WT littermates.

147   We bred our conditional G34D allele ($Ski^{G34D/+:Neo}$) mouse line to transgenic mice carrying

148   the vascular smooth muscle cell (VSMC) specific Sm22α-Cre driver (32), to generate mice that

149   selectively expressed mutant SKI only in VSMC populations. These mice ($Ski^{VSMC:G34D/+}$) also

150   showed evidence of aortic root aneurysm at 6 months of age compared to WT littermates, and

151   increased post-natal aortic root growth between 2 and 6 months of age, that was indistinguishable

152   from the rate of growth seen in $Ski^{G34D/+}$ mice, which ubiquitously express mutant Ski (Fig. 1D,

153   S1A).

154   As previously observed in dermal fibroblasts from patients with SGS (21), qPCR of aortic

155   tissue taken from $Ski^{G34D/+}$ and $Ski^{VSMC:G34D/+}$ mice showed increased expression of all assayed

156   TGFβ target genes, including $Col3A1, Fn1, Smad7, Mmp2, Col1A1, Cdkn1a, Ctgf, Serpine1, Skil,$

157    $and\ Mmp9$ (encoding type 3 collagen, fibronectin, SMAD family member 7, matrix

158   metallopeptidase 2, type 1 collagen, p21, connective tissue growth factor, PAI-1, SKI-like protein,

159   and matrix metallopeptidase 9, respectively; Fig. 1E, S2).

160   These data confirm that this knock-in mouse model of SGS recapitulates multiple

161   phenotypic manifestations of the disorder seen in humans, and that the aortic root aneurysm seen

162   in these mice associates with increased TGFβ-dependent target gene expression in the aortic wall.

163   The absence of a phenotype in $Ski^{G34D/+:Neo}$ mice supports the conclusion that the SGS phenotype

164   does not manifest as a result of Ski haploinsufficiency, leaving open the possibility of either a

165   dominant negative mechanism of action or a novel gain of function.

166

167 *Angiotensin-2 type 1 receptor blocker (ARB) losartan ameliorates aortic aneurysm growth in SGS*

168 *mice*

169 The ARB losartan has previously been shown to ameliorate aortic root aneurysm

170 progression in mouse models of both MFS and LDS, in association with blunted Smad2/3 and

171 Erk1/2 activation (8, 9). To investigate the potential therapeutic effect of losartan in SGS, 2-month

172 old $Ski^{G34D/+}$ and $Ski^{VSMC:G34D/+}$ mice were treated for 4 months with a dose of losartan previously

173 shown to be efficacious in MFS and LDS mice. Aortic root size was measured at 2 months of age

174 (pre-treatment baseline) and every month thereafter until 6 months of age. Aortic root growth was

175 significantly greater in placebo-treated $Ski^{G34D/+}$ and $Ski^{VSMC:G34D/+}$ mice compared with WT

176 littermates (Fig. 2A, S3A).

177 Compared to placebo-treated $Ski^{G34D/+}$ and $Ski^{VSMC:G34D/+}$ littermates, aortic root growth was

178 significant reduced in losartan-treated $Ski^{G34D/+}$ and $Ski^{VSMC:G34D/+}$ mice to a rate indistinguishable

179 from that observed in control mice. No significant change in total body weight was observed with

180 losartan treatment (Fig. S3B). ARBs such as losartan lower blood pressure, which is known to be

181 beneficial in slowing aortic aneurysm growth. To investigate whether losartan was achieving its

182 protective effect solely through blood pressure reduction, we performed a head-to-head trial with

183 another antihypertensive agent, the beta-blocker atenolol. $Ski^{G34D/+}$ and $Ski^{VSMC:G34D/+}$ mice and

184 control littermates were treated with hemodynamically-equivalent doses of either atenolol

185 (60mg/kg/day) or losartan (50mg/kg/day), from 2 to 6 months of age. Aortic root growth during

186 this 4 month period in atenolol-treated $Ski^{VSMC:G34D/+}$ mice was significantly less than that of

187 placebo-treated $Ski^{VSMC:G34D/+}$ mice (Fig. S3C), as expected following blood pressure reduction.

188 By contrast, losartan-treated $Ski^{VSMC:G34D/+}$ mice showed a significantly greater reduction in aortic

189 root growth when compared to atenolol-treated $Ski^{VSMC:G34D/+}$ mice, despite an equivalent

9

190   reduction in blood pressure and no significant change in total body weight with the 2 drugs (Fig.

191   S3C, D, E)

192   Histological and morphometric analyses of aortic wall cross sections were performed

193   following death or sacrifice of the mice at 6 months of age. Verhoeff-Van Gieson (VVG) and

194   trichrome staining displayed evidence of aortic wall thickening due to massive accumulation of

195   collagen in the aortic media, reduced elastin content, and increased elastic fiber fragmentation in

196   placebo-treated *Ski*$^{G34D/+}$ and *Ski*$^{VSMC:G34D/+}$ mice, compared with WT littermates, all of which were

197   normalized by losartan treatment (Fig. 2B, C, D).

198   To further confirm that losartan was achieving its effect through a mechanism other than

199   simple blood pressure reduction, we assessed TGFβ-dependent target gene expression in the aortas

200   of 6-month old mice. Placebo-treated *Ski*$^{G34D/+}$ mice and *Ski*$^{VSMC:G34D/+}$ mice showed a significantly

201   greater expression of TGFβ-dependent target genes, compared with WT littermates (Fig. 2E, S2).

202   By contrast, losartan treatment led to a significant reduction in the expression of these genes in

203   *Ski*$^{G34D/+}$ mice and *Ski*$^{VSMC:G34D/+}$ mice, to levels indistinguishable from those seen in WT

204   littermates in most instances. These data support the conclusion that ARB blockade with the use

205   of losartan appears highly efficacious in treating aortic aneurysm growth in knock-in mouse

206   models of SGS, in association with reduced TGFβ-dependent gene expression, analogous to what

207   has been observed in mouse models of both MFS and LDS (8, 9). It may hence represent a novel

208   therapeutic strategy for the treatment of patients with SGS.

209

210   *Selective CBP/P300 inhibition rescues aortic aneurysm growth in SGS mice*

211   The G34D mutation is located in the R-SMAD binding domain of SKI. Interestingly, a

212   mutated form of SKI lacking this R-SMAD binding domain was found to retain its ability to

213   regulate SMAD-mediated transcriptional activation in a transient transfection reporter assay, but

214   failed to dissociate CBP/P300 from the SMAD complex (**28, 30**). Indeed, SKI and CBP/P300 are

215   known to compete for binding to R-SMADs, and binding of SKI to R-SMADs is sufficient to

216   displace CBP/P300, an effect that is not mimicked by the interaction of SKI with SMAD4.

217   Maintenance of CBP/P300 within the complex promotes gene expression via increased H3K27

218   acetylation and hence preservation of an open chromatin state (**33-39**). An increase is resident

219   CBP/P300 can also positively regulate transactivation activity through acetylation of the MH2

220   domain of SMAD3 at lysine 378 (40). Our prior phenotyping data confirmed that

221   haploinsufficiency for SKI does not appear to be the mechanism of action in SGS. We therefore

222   hypothesized that SGS-causing missense mutations in the R-SMAD binding domain of SKI might

223   allow maintenance of CBP/P300 binding despite residual recruitment of SKI to regulatory

224   elements in target genes via interaction with SMAD4. The resulting increase in H3K27 acetylation

225   and heightened and/or prolonged TGFβ-dependent gene transcription would not manifest in

226   experimental systems that are not susceptible to this type of epigenetic regulation.

227   To investigate this, we first performed immunofluorescence staining to look for evidence of

228   enhanced H3K27 acetylation in the aortic root of $Ski^{VSMC:G34D/+}$ mice at 6 months of age. Compared

229   with control littermates, $Ski^{VSMC:G34D/+}$ mice did indeed show much greater H3K27 acetylation in

230   the medial layer of the aortic root (Fig. 3A). To confirm that increased H3K27 acetylation is a

231   driver of aortic aneurysm progression in SGS, rather than simply a marker of it, we treated

232    $Ski^{VSMC:G34D/+}$ mice with the selective CBP/P300 inhibitor C646 (**41**). Treatment with C646 (1

233   mg/kg/day) was started at 2 months of age and continued for 3 months until sacrifice of the mice

234   at 5 months of age. Control mice were treated with the vehicle dimethyl sulfoxide (DMSO) alone.

235   Aortic root size was measured at 2 months of age (pre-treatment baseline) and every month

236   thereafter. Aortic root growth during the treatment period was significantly greater in vehicle-

237   treated $Ski^{VSMC:G34D/+}$ mice, compared with control littermates (Fig. 4A, S4A), and was comparable

238   to that previously seen in placebo-treated $Ski^{VSMC:G34D/+}$ mice. By contrast, C646 treatment led to

239   a significant reduction in aortic root growth in $Ski^{VSMC:G34D/+}$ mice, to a rate indistinguishable from

240   that observed in control mice, without a change in total body weight (Fig. S4B). Importantly, C646

241   therapy had no effect in control mice, showing that inhibition of H3K27 acetylation was selectively

242   targeting Ski mutation-associated pathological aortic root growth rather than physiological aortic

243   growth.

244   The specificity of C646 was confirmed by immunofluorescence staining for H3K27

245   acetylation. Compared with DMSO-treated $Ski^{VSMC:G34D/+}$ littermates, C646-treated $Ski^{VSMC:G34D/+}$

246   mice showed a clear reduction in H3K27 acetylation in the medial layer of the aortic root (Fig.

247   3A). Histological and morphometric analyses of aortic wall cross sections were performed

248   following death or sacrifice of the mice at 5 months of age. VVG and trichrome staining

249   reconfirmed prominent aortic wall thickening, reduced elastin content, and increased elastic fiber

250   fragmentation in vehicle-treated $Ski^{VSMC:G34D/+}$ mice compared to control littermates, all of which

251   were significantly improved in C646-treated $Ski^{VSMC:G34D/+}$ mice (Fig. 3B, C, D).

252   To determine whether this reduction in H3K27 acetylation by C646 directly impacted

253   TGFβ-dependent gene expression in the aortas of these mice, we performed qPCR on the aortas

254   of 5-month old mice. The increased expression of TGFβ target genes seen in vehicle-treated

255   $Ski^{VSMC:G34D/+}$ mice was indeed significantly reduced in C646-treated $Ski^{VSMC:G34D/+}$ mice, to

256   levels close to or indistinguishable from those seen in control mice (Fig. 4B, S5). To confirm that

257   C646 does not have any antihypertensive effect, we measured blood pressure in these animals and

12

258 found no significant difference between vehicle-treated $Ski^{VSMC:G34D/+}$ mice and C646-treated

259 $Ski^{VSMC:G34D/+}$ littermates (Fig. S4C).

260 These data suggest that missense mutations in the R-SMAD domain of SKI lead to enhanced

261 CBP/P300 activity, increased H3K27 acetylation, and ultimately prolonged TGFβ-dependent gene

262 expression, all of which can be ameliorated in a mouse model of SGS by selective CBP/P300

263 inhibition. Since animal models of MFS, in particular the $Fbn1^{C1039G/+}$ mouse model, also show

264 increased TGFβ-dependent gene expression in their aortas, we hypothesized that selective

265 CBP/P300 inhibition could represent a novel therapeutic strategy for other forms of inherited aortic

266 aneurysm. To assess this, we treated $Fbn1^{C1039G/+}$ mice with C646 from 2 months of age for 2

267 months. Aortic root growth over the treatment period was significantly greater in vehicle-treated

268 $Fbn1^{C1039G/+}$ mice than WT littermates (Fig. 4C). By contrast, C646 treatment led to a significant

269 reduction in aortic root growth in $Fbn1^{C1039G/+}$ mice, to a rate comparable to that observed in WT

270 controls. This reduction in aortic root growth was associated with a significant reduction in TGFβ-

271 dependent gene expression in C646-treated $Fbn1^{C1039G/+}$ mice, compared to their vehicle-treated

272 littermates (Fig. 4D).

273

274 *CBP/P300 inhibition abrogates TGFβ-dependent gene expression in SGS patient cells*

275 We tested the effect of C646 on primary dermal fibroblasts derived from 2 SGS patients and

276 2 healthy controls. Vehicle-treated fibroblasts from SGS patients showed significantly greater

277 mRNA expression of TGFβ-dependent genes, including *COL3A1, FN1, SKI,* and *SMAD7*,

278 compared with control fibroblasts, both at baseline and after stimulation with exogenous TGFβ1

279 (10 ng/ml) for 6 hours (Fig. S6). By contrast, C646 treatment of SGS patient fibroblasts led to a

280 significant reduction in expression of these genes, to levels similar to those seen in control

13

281   fibroblasts, or SGS patient fibroblasts treated with the TGFβ type I receptor (Alk5) kinase inhibitor

282   SD208. Selective CBP/P300 inhibition thus appears to suppress TGFβ-dependent gene expression

283   in both mouse models of SGS and cells derived from patients with SGS.

284

Discussion

Shprintzen-Goldberg syndrome (SGS) in a rare systemic connective tissue disorder caused by heterozygous mutations in the *SKI* gene, and shows significant phenotypic overlap with both MFS and LDS. Despite the initial discovery of a causal gene, a number of questions remained unanswered about the disorder, including the effect of SGS-causing mutations on TGFβ signaling in vivo, the exact role of TGFβ signaling in the disease, and which SKI binding partners and downstream signaling sequelae contribute to pathogenesis.

The body of evidence implicating dysregulation of TGFβ signaling in vascular connective tissue disorders is extensive and compelling. Virtually every study of these conditions has provided evidence for high TGFβ signaling in the aortic wall of mouse models or people with MFS or LDS, including enhanced activation of signaling intermediates (i.e. phosphorylation and/or nuclear translocation of SMAD2/3) and high output of TGFβ target genes in relevant tissues. Yet ambiguity is demonstrable and controversy substantial. Evidence suggested that fibrillin-1, the deficient gene product in Marfan syndrome, could positively regulate TGFβ signaling by concentrating cytokine at sites of intended function, but negatively regulate signaling by sequestering the TGFβ latent complex from activators (5, 42-44). All forms of LDS are caused by heterozygous loss-of-function mutations in genes encoding positive effectors of TGFβ signaling (4, 17, 45-47). Therapeutic trials were equally ambiguous. While the consistent therapeutic benefit of ARBs in mouse models of MFS or LDS strictly correlated with attenuation of the tissue signature for high TGFβ signaling in the aortic wall, administration of TGFβ neutralizing antibodies accentuated disease in the perinatal period in MFS mice, while affording significant protection later in postnatal life, with heightened efficacy when used in combination with ARBs (9). The fact SGS includes essentially every systemic manifestation of MFS (except

15

308   lens dislocation) and LDS seemed particularly relevant given the prominent role of SKI in the

309   negative regulation of the TGFβ transcriptional response (1, 2, 21, 48). The observations that

310   SGS mutations clustered in the R-SMAD binding domain of SKI, and that SGS patient fibroblasts

311   showed high expression of TGFβ-responsive genes known to contribute to aneurysm progression

312   suggested that increased TGFβ-dependent events may cause the multisystem manifestations of

313   SGS. This might also inform the mechanism for similar manifestations in MFS and LDS.

314   More recently, it was reported by Hill and colleagues that SGS mutations can promote

315   enhanced stability of SKI, and that this was associated with decreased expression of selected TGFβ

316   target genes in either cells transfected with mutant SKI or in SGS fibroblasts (31). Notably, this

317   study only assessed the acute phase-response to administered TGFβ ligand (1 and 8 hours after

318   delivery), and focused on genes that are predominantly expressed in neurons or polarized epithelial

319   cells, but not the aortic wall or dermal fibroblasts. Prior work had demonstrated that loss of binding

320   of SKI to R-SMADs, as imposed by SGS mutations, did not abrogate the regulation of the TGFβ

321   transcriptional response in reporter allele assays, but rather impaired the ability of SKI to displace

322   CBP/P300 at critical regulatory elements, potentially altering the efficiency of chronic SKI-

323   mediated termination of a signal initiated by TGFβ (28, 30). This effect would be best interrogated

324   upon chronic exposure to TGFβ, with potentially unique insights afforded by the study of affected

325   tissues in vivo. Moreover, the impact of an SGS mutation could vary based upon cell type, with

326   particular relevance for the expression of redundant negative regulators (e.g. SKIL or SMAD7) or

327   factors involved in chronic compensation. Importantly, our prior studies in dermal fibroblasts

328   derived from SGS patients assessed TGFβ target gene expression at steady-state, with no overlap

329   between the repertoire of genes previously assessed and those specifically examined by Hill and

330   colleagues (21, 31). We now unequivocally show that constitutive or VSMC-specific expression

16

331   of a heterozygous SGS-associated SKI mutation leads to a substantial and sustained increase in

332   H3K27 acetylation in vivo, as predicted by increased CBP/P300 occupancy, in association with

333   high expression of TGFβ target genes relevant to aortic disease and reliably assayed in dermal

334   fibroblasts. These findings correlated with the excessive accumulation of fibrillar collagens in the

335   vessel wall and skin of SGS mouse models, as predicted by amplification of the TGFβ

336   transcriptional response, with notable downregulation appearing coincident with therapeutic

337   interventions that achieved attenuation of aneurysm progression.

338   These data are consistent with prior work showing that CBP/P300-mediated H3K27

339   acetylation is enriched in the promoter regions of TGFβ target genes (49). Furthermore,

340   CBP/P300-mediated histone acetylation at the PAI-1 and p21 promoters can enhance TGFβ1-

341   induced expression of these genes in cell culture systems (50). By contrast, CBP/P300 inhibition

342   using C646 has been shown to significantly reduce H3K27 acetylation (51), and also abrogate

343   expression of a number of TGFβ target genes, including *Cdkn1a*, *Mmp*, *Serpine1* and *Ctgf* (52-

344   55). Prior work has shown that C646 can have a substantial effect on behavioral characteristics in

345   rodents such fear memory (56, 57), and on cardiac fibrosis and hypertrophy in *Sirt3* deficient mice

346   (58). Although we have shown efficacy of C646 against aortic aneurysm progression in SGS and

347   MFS mice, its therapeutic potential for other systemic manifestations of these vascular connective

348   tissue disorders remains untested.

349   ARBs such as losartan have previously been shown to attenuate TGFβ signaling through

350   downregulation of TGFβ ligands, receptors and activators such as PAI-1 (9, 11). The overt

351   protection from aneurysm progression seen in mouse models of MFS and LDS associates with a

352   reduction in TGFβ signaling in the aortic root media, as evidenced by normalization of SMAD2/3

353   phosphorylation and the expression of TGFβ target genes in the aortic wall, prominently including

17

354   fibrillar collagens, MMPs 2 and 9 and CTGF (7, 8, 11). A role for losartan in epigenetic

355   modulation of the TGFβ transcriptional response is less clear. Work by Reddy et al. has shown

356   that losartan can ameliorate diabetic nephropathy in mice through a reduction in H3K9/14

357   acetylation at the promoters of pathogenic genes (59). Furthermore, losartan was found to

358   attenuate proteinuric kidney disease in mice via inhibition of DNA methylation at the nephrin

359   promoter (60). The relative importance of each of these potential mechanisms of action for ARBs

360   in SGS remains to be determined. Our current hypothesis is that ARBs predominantly suppress

361   early events in TGFβ signaling, precluding abnormal maintenance and/or amplification of the

362   transcriptional response in the context of a SKI functional deficiency.

363   Given the known phenotypic overlap, and the newly-confirmed biochemical similarity,

364   between SGS and both MFS and LDS, a logical extension of this work was to elucidate whether

365   epigenetic changes and their pharmacological manipulation may hold relevance to other CTDs.

366   Indeed, treatment with C646 did lead to a significant reduction in aortic root growth in MFS mice,

367   in association with reduced TGFβ target gene expression in the aortic wall. This suggests that a

368   reduction in H3K27 acetylation can achieve a therapeutic effect, likely by facilitating a more

369   closed chromatin state that impairs TGFβ target gene transcription, despite the presence of

370   increased upstream TGFβ signaling. The findings of this study suggest that epigenetic modulation

371   holds potential for the treatment in diverse presentations of syndromic forms of aortic aneurysm.

372   These data add to the extensive and compelling in vivo evidence for enhanced TGFβ

373   signaling in the pathogenesis of vascular connective tissue disorders including MFS, LDS and SGS,

374   with particular emphasis on the vascular pathology. In comparison, there is no documented

375   example of decreased TGFβ signaling in tissues derived from people or mouse models of these

376   conditions. Yet, we view the evidence for primary functional impairment of the TGFβ signaling

377   response by underlying mutations to be equally compelling, including the evidence by Hill and

378   colleagues that SGS mutations can stabilize SKI and associate with relative impairment of

379   transcriptional responses in selected culture systems (31). The challenge – and, we would argue,

380   the opportunity - lies in embracing all inconvenient truths to arrive at reconciling and testable

381   models that have the true potential to inform disease pathogenesis and therapeutic opportunities.

382   In the case of LDS, we have shown that heterozygous loss-of-function mutations in positive

383   effectors of TGFβ signaling have a disproportionate and at times even unique negative impact on

384   responses in specific cell types (12). This can lead to paracrine effects (e.g enhanced TGFβ ligand

385   production) that drive excessive signaling in neighboring cell types that are less vulnerable to the

386   consequences of underlying mutations (12). Given the potency and redundancy of mechanisms for

387   autoregulation of TGFβ signaling, it seems possible that the apparent low signaling – high

388   signaling paradox in the TGFβ vasculopathies is actually a requirement for the initiation and

389   maintenance of a high TGFβ signaling state. There is ample precedent for this in the TGFβ cancer

390   paradox, where TGFβ serves both as a tumor suppressor and a positive regulator of tumor

391   progression. We anticipate that consideration and integration of this physiologic complexity will

392   be required to achieve consensus – and truth – in our field.

393

394 **Methods**

395 *Mouse lines*

396   All mice were cared for under strict compliance with the Animal Care and Use Committee

397 of the Johns Hopkins University School of Medicine. $Ski^{G34D/+}$ mice were generated by

398 homologous recombination, as described in the next section. $Ski^{tm1a(EUCOMM)Hmgu}$ (tm1a represents

399 targeted mutation 1a, and hmgu represents Helmholtz Zentrum Muenchen GmbH) embryonic stem

400 cells were obtained from the European Conditional Mouse Mutagenesis Program and injected into

401 the cavity of day 3.5 blastocysts from C57BL/6J mice at the Johns Hopkins University School of

402 Medicine transgenic core. Male chimeras were mated with C57BL/6J WT female mice to establish

403 germline transmission. The *LacZ*-Neo cassette was removed by crossing with a FlpO transgenic

404 strain (B6.Cg-Tg(Pgk1-flpo)10Sykr/J, #011065) purchased from the Jackson Laboratory and to

405 generate $Ski^{+/-}$ mice, exon 2 and 3 of *Ski* gene flanking by *loxP* sequences were removed by

406 crossing with a transgenic Cre strain (B6.C-Tg(CMV-cre)1Cgn/J, #006054) purchased from the

407 Jackson Laboratory, followed by mating to the C57BL/6J strain at least 5 generations. Sm22α-Cre

408 mice (B6.Cg-Tg(Tagln-cre)1Her/J, #017491) were purchased from the Jackson Laboratory,

409 followed by mating to the C57BL/6J strain for at least 5 generations. To minimize potentially

410 confounding background effects, all comparisons between genotypes and between treatment arms

411 within a genotype were made between gender-matched littermates.

412   Mice were checked daily for evidence of premature lethality. At the end of a drug trial, all

413 mice were euthanized through inhalational halothane (Sigma) or anesthetized with isofluorane.

414 Following sacrifice, mice underwent immediate laparotomy, descending abdominal aortic

415 transection, and phosphate-buffered saline (PBS; pH 7.4) was infused throughout the vascular tree

416 via the left ventricle. For the aorta frozen section, additional 4% paraformaldehyde in PBS was

20

417   infused again for fixation tissue. Sacrificed mice used for 3 harvest methods, latex infusion for

418   histological analysis, freezing heart and aorta embedded in optimal cutting temperature compound

419   (O.C.T compound) for immunofluorescent staining, and *in-situ* hybridization and snap-frozen

420   aorta in liquid nitrogen.

421   For quantitative RT-PCR, the aortic root and ascending aorta (above the aortic root to the

422   origin of right brachiocephalic trunk) of mice were harvested separately, snap-frozen in liquid

423   nitrogen, and stored at -80°C until processed. For RNA extraction, aortas were homogenized in

424   TRizol (ThermoFisher) by FastPrep-24 (MP Biomedicals, LLC), per the manufacturer's

425   instructions. After homogenization, RNA was extracted using an RNeasy mini kit (QIAGEN), per

426   the manufacturer's instructions. The RNA samples were then stored once more at -80°C until

427   quantitative RT-PCR was performed.

428   For the frozen aorta sections, aorta with heart was harvested and fixed in fresh 4%

429   paraformaldehyde in PBS at 4°C overnight, and then placed in cold 30% sucrose in PBS solution

430   and incubated at 4°C overnight again. Tissue was then embedded in Tissue-Tek O.C.T compound

431   and snap-frozen in liquid nitrogen, and stored at -80°C until processed.

432   According to a previously described protocol with slight modification (7, 11, 61) mice that

433   were analyzed for aortic histology had latex infused into the left ventricle through the descending

434   abdominal aorta. Mice were then fixed for 24 hours in 10% neutral-buffered formalin, before being

435   stored in 70% ethanol until the histological analysis was performed.

436

437   *Generation of Ski $^{G34D/+}$ mice*

438   *Ski* $^{G34D/+}$ mice were generated by homologous recombination. A 10-kb *Ski* fragment was

439   generated by PCR from mouse embryonic stem cell DNA. The amplicon was subcloned into

440 pCR2.1-TOPO (Invitrogen Corp.). Site-directed mutagenesis was performed with the In-Fusion

441 HD kit (Clontech Inc.), creating G34D mutation. The Neo cassette was amplified from pMC1neo-

442 polyA vector (Stratagene Inc.) and the fragment containing the *Sal*1 restriction site and Neo

443 cassette with flanking *loxP* sequences was subcloned into a unique *Sal*1 site in the *Ski* intron after

444 exon 1. All targeting vector sequences, including the sequences of the *loxP* sites and site-directed

445 mutagenesis-created mutations were confirmed by sanger sequencing. The vector was linearized

446 using a unique (*EcoR*1) site and electroporated into R1 embryonic stem cells. Positive clones were

447 identified by PCR test. Positives clones were injected into 129S6/ScEvTac blastocysts at

448 embryonic day 3.5 and transferred into pseudopregnant females. Chimeric offspring were mated

449 to C57BL/6J mice, and germline transmission was observed for at least 3 independent targeting

450 events for mutant genotype. All exons encompassed by and immediately flanking the targeting

451 vector were analyzed by sequencing of PCR-amplified genomic DNA derived from mutant mice,

452 to demonstrate the fidelity of targeting. Mice were genotyped on the basis of creation of a new

453 *BamH*1 site in correctly targeted mice. Primers used for amplification were 5'–GAGCCCGATCG

454 CACCATGGAA-3' (sense) and 5'-AAGAGATGGTCTCCCCTTCC-3' (antisense). For testing

455 the random insertion of linearized targeted vector, quantitative PCR of the Neo cassette sequence

456 was performed with a previously verified DNA sample, which contained only a single Neo cassette

457 sequence. The *loxP*-flanked Neo cassette was removed by crossing with a Cre deleter strain, either

458 CMV-Cre (B6.C-Tg(CMV-cre)1Cgn/J, #006054) purchased from the Jackson Laboratory,

459 followed by mating to C57BL/6J strain for at least 5 generations for a C57BL/6J genetic

460 background, or Prm-Cre (129S/Sv-Tg(Prm-Cre)58Og/J, #003328) purchased from Jackson

461 Laboratory, followed by mating to a 129S6/ScEvTac strain for at least 5 generations for a

462 129S6/ScEvTac genetic background. The 129S6/ScEvTac genetic background *Ski* $^{G34D/+}$ mice

463   were used for analyses of dermal, skeletal, and cardiovascular phenotypes. The C57BL/6J genetic

464   background *Ski* ^{G34D/+} mice were used for behavioral phenotype analysis. *Ski* ^{G34D/+:Neo} mice were

465   bred to the 129S6/ScEvTac strain for at least 5 generations, without deletion of the Neo cassette

466   as a separate mouse line. Complete concordance of phenotype for 3 or 2 independent lines and

467   backcrossing to each congenic inbred strain for at least 5 generations excluded any major off-target

468   effects.

469

470   *Mouse drug treatment*

471   Losartan was dissolved in drinking water and filtered to reach a concentration of 0.5 g/L,

472   giving an estimated daily dose of 50 mg/kg/day (based on a 30-g mouse drinking 3 mLs per day).

473   Atenolol was dissolved in drinking water and filtered to reach a concentration of 0.6 g/L, giving

474   an estimated daily dose of 60 mg/kg/day. Placebo-treated mice received drinking water. Mice

475   given these medications were started on treatment at 8 weeks of age and continued for 16 weeks.

476   C646 (Selleckchem, #S7152) was reconstituted in 10% DMSO (Sigma) dissolved in PBS, and

477   administered daily by intraperitoneal injection at a dose of 1 mg/kg/day. Treatment was initiated

478   at 8 weeks of age and continued for 12 weeks. Ten percent DMSO in PBS was administered as a

479   control.

480

481   *Mouse echocardiography*

482   Nair hair removal cream was used to remove fur from the anterior thorax of the mice the

483   day prior to echocardiography. According to a previous protocol with slight modifications (7, 11,

484   61), echocardiography was performed on awake, nonsedated mice using a Vevo 2100 imaging

485   system and 40 MHz transducer (Visualsonics). Mice were imaged at 8 weeks of age as a baseline

23

486 and every 4 weeks thereafter, until 20 weeks of age. The aorta was imaged in the parasternal long-

487 axis view. Three separate measurements of the maximal internal dimension at the sinus of Valsalva

488 during systole were made in separate cardiac cycles and averaged. All imaging and analysis was

489 performed blinded to genotype and treatment arm.

490

491 *Mouse blood pressure*

492 According to a previously described protocol with slight modifications (7, 11, 61), blood

493 pressure was measured by tail-cuff plethysmography using a Harvard Apparatus IITC noninvasive

494 tail cuff device. Mice were placed in a standard acrylic restrainer for adult mice, with an internal

495 diameter of 25 mm and an adjustable head gate. The end plate was removable, allowing the mice

496 to walk into the restrainer without using force. Hemodynamic recordings were made without

497 sedation or anesthesia. Blood pressure was measured at the end of the drug trial. Mice were

498 habituated for 4 days. On day 5, ten blood pressures were obtained and averaged.

499

500 *Mouse radiography*

501 According to a previously described protocol with slight modifications (7, 11, 61), Mice

502 were anesthetized using a combination of 50 mg/kg of ketamine-HCl and 5 mg/kg xylazine-HCl

503 by intraperitoneal injection before X-ray imaging. Mice were placed in the left lateral decubitus

504 position on a radiolucent platform with a metal paper clip as a scale bar and imaged at 1x

505 magnification using a Faxitron MX20 (Faxitron).

506

507 *Mouse aorta histological analysis*

508   According to a previously described protocol with slight modifications (7, 11, 61), latex-

509   infused heart and aorta were removed from body and transected just below the level of the aortic

510   annulus, and just above the aortic root, and 2- to 3-mm transverse sections were mounted in 4%

511   agar prior to fixation in paraffin. Five-micron aortic sections underwent Verhoeff-van Giesen

512   (VVG) and Masson's trichrome staining and were imaged at 40x magnification using a Nikon

513   Eclipse E400 microscope. Aortic wall thickness was measured of 4 sites of 4 representative

514   sections for each mouse. The disruptions of elastin fiber architecture were counted in 4 sections

515   every 25 microns from the aortic annulus. All analyses were performed blinded to genotype and

516   treatment arm and the results were averaged.

517

518   *Mouse behavioral tests*

519   Behavioral tests were performed per the manufacturer's instructions. All of behavioral tests

520   were performed at 10 weeks of age. For the open field test, a mouse was placed into a corner of a

521   45 x 45 cm open-filed chamber (San Diego Instruments) with a 16 x 16 photobeam configuration.

522   The behavior of the mouse was monitored for 5 minutes in each of 6 cycles (total 30 minutes).

523   Mouse activity in center area and/or peripheral areas was recorded by beam interruptions. Total

524   activity was calculated by adding up all beam interruptions during the cycle. Activity in the central

525   and peripheral areas was calculated by adding up the beam interruptions in these two areas,

526   respectively. For the rotarod test, mice were placed on a horizontally oriented, rotating cylinder

527   (rod) suspended above the cage floor (Rotamex-5 rotarod, Columbus Instruments). The

528   acceleration started at 0 rpm and was increased by 1.0 rpm every 5 seconds. Velocity and time

529   were recorded at the time of falling for 3 measurements. Each mouse was given 3 minutes of rest

530   time between trials. All analyses were performed blinded to genotype and the results were

531   averaged.

532

533   *Human cell culture*

534   Primary human dermal fibroblasts were derived from forearm skin biopsies of 2 controls

535   and 2 patients with SGS, as previously described in (21). The fibroblasts were cultured in

536   Dulbecco's modified eagle medium (DMEM) with 10% fetal bovine serum (FBS) in the presence

537   of antibiotics and passaged confluence. According to a previously described protocol with slight

538   modifications (21), all cell culture experiments were conducted in serum-starved media for 24

539   hours prior to drug treatment. Stimulation was performed using 10 ng/ml recombinant human

540   TGFβ1 (R&D system). C646 dissolved in DMSO was treated at a dose of 20 μM for 24 hours of

541   pretreatment before TGFβ1 stimulation. SD208 dissolved in DMSO was treated at a dose of 10

542   μM for 24 hours of pretreatment before TGFβ1 stimulation. Cells were collected at baseline, 6

543   hours after TGFβ1 stimulation. The RNA was extracted from the cells using TRizol

544   (ThermoFisher) via an RNeasy mini kit (QIAGEN), per the manufacturer's instructions.

545

546   *Quantitative RT-PCR expression analysis*

547   Total RNA was isolated from mouse aortas or cultured cells using an RNeasy mini kit

548   (QIAGEN), per the manufacturer's instructions. Quantitative PCR was performed in triplicate with

549   TaqMan Universal PCR Master Mix using an ABI Prism 7900 HT QPCR machine (all from

550   Applied Biosystems), per the manufacturer's instructions. The following prevalidated TaqMan

551   probes were used to detect specific transcripts: Mm00801666_g1 (*Col1a1*), Mm01254476_m1

552   (*Col3A1*), Mm01256744_m1 (*Fn1*), Mm04205640_g1 (*Cdkn1a*), Mm01192932_g1 (*Ctgf*), and

553   Mm00435860_m1 (*Serpine1*), Mm00448744_m1 (*Ski*), Mm00456917_m1 (*Skil*),

554   Mm00484742_m1 (*Smad7*) and Mm00607939_s1 (*Actb*) (Life Technologies). For human samples,

555   the following probes were used: Hs00943809_m1 (*COL3A1*), Hs00365052_m1 (*FN1*),

556   Hs00161707_m1 (*SKI*), Hs01045418_m1 (*SKIL*) and Hs01060665_g1 (*ACTB*). Reactions were

557   run in triplicate, and relative quantification for each transcript was obtained by normalization

558   against a housekeeping control transcript, such as *β–ACTIN* (*ACTB*), according to the formula $2^{-Ct}/2^{-Ct(ACTB)}$.

559

560

561   *Immunofluorescence*

562   Immunofluorescence was performed as previous described (**8**, **9**). Frozen 10-μM long-axis–

563   view sections were obtained with a cryostat and mounted on glass slides. Sections were dried at

564   room temperature overnight prior to staining. Sections were permeabilized in staining buffer (PBS

565   containing 0.1% Triton-X 100) for 30 minutes and then incubated with Fc Receptor Block from

566   Innovex for 30 minutes at room temperature, washed briefly in staining buffer, and then incubated

567   again in blocking solution (0.1% Triton-X 100, 1:50 goat serum, 0.3M glycine) for 30 minutes.

568   Primary antibodies were diluted at 1:100 in staining buffer and incubated with goat anti-rabbit

569   secondary antibody conjugated to Alexa Fluor 555 (Life Technologies) at 1:200 for 1 hour before

570   being mounted with VECTASHIELD Hard Set Mounting Medium with DAPI. Images were

571   acquired on a Zeiss Axio Examiner with a 710NLO-Meta multiphoton confocal microscope at 25*x*

572   magnification. The following primary antibody was used: anti-H3K27ac (Abcam, ab4729).

573

574   *Statistics*

575   All quantitative data are shown as bar graphs, produced using Graphpad Prism. Mean ±

576   standard errors of the mean (SEM) are displayed. Statistical analyses were performed using non-

577   parametric test (Kruskal-Wallis test with Dunn's multiple comparison test). A P value < 0.05 was

578   considered to be statistically significant for all tests.

579

580   *Study approval*

581   This study was performed in accordance with the recommendations in the Guide for the

582   Care and Use of Laboratory Animals of the National Institutes of Health. All of the animals were

583   handled according to approved institutional animal care and use committee (IACUC) protocols

584   of the Johns Hopkins University School of Medicine. The protocol was approved by the

585   Committee on the Ethics of Animal Experiments of the Johns Hopkins University School of

586   Medicine.

587

Author contributions

H.C.D and B.E.K. developed the concept. B.E.K. generated mouse models, designed, performed and directed experiments, analyzed data and wrote the manuscript. J.J.D., E.G.M., and H.C.D. aided in experimental design and interpretation of the data. R.B. aided in mouse colony maintenance and drug treatment. D.B. aided in mouse echocardiography and analyses. R.B., J.J.D., E.G.M., and H.C.D provided essential expertise in the editing of the manuscript. All authors discussed the results and commented on the manuscript prior to submission.

References

1. Schepers D et al. The SMAD-binding domain of SKI: a hotspot for de novo mutations causing Shprintzen–Goldberg syndrome. *Eur J Hum Genet* 2014;23(2):1–5.

2. Pagon RA et al. Shprintzen-Goldberg Syndrome1993;

3. Dietz HC et al. Marfan syndrome caused by a recurrent de novo missense mutation in the fibrillin gene. *Nature* 1991;352(6333):337–339.

4. Loeys BL et al. A syndrome of altered cardiovascular, craniofacial, neurocognitive and skeletal development caused by mutations in TGFBR1 or TGFBR2. *Nat Genet* 2005;37(3):275–281.

5. Neptune ER et al. Dysregulation of TGF-beta activation contributes to pathogenesis in Marfan syndrome. *Nat Genet* 2003;33(3):407–411.

6. Judge DP et al. Evidence for a critical contribution of haploinsufficiency in the complex pathogenesis of Marfan syndrome. *J. Clin. Invest.* 2004;114(2):172–181.

7. Holm TM et al. Noncanonical TGF Signaling Contributes to Aortic Aneurysm Progression in Marfan Syndrome Mice. *Science* 2011;332(6027):358–361.

8. Gallo EM et al. Angiotensin II-dependent TGF-β signaling contributes to Loeys-Dietz syndrome vascular pathogenesis. *J. Clin. Invest.* 2014;124(1):448–460.

9. Habashi JP et al. Losartan, an AT1 Antagonist, Prevents Aortic Aneurysm in a Mouse Model of Marfan Syndrome. *Science* 2006;312(5770):117–121.

10. Cohn RD et al. Angiotensin II type 1 receptor blockade attenuates TGF-β–induced failure of muscle regeneration in multiple myopathic states. *Nat Med* 2007;13(2):204–210.

11. Habashi JP et al. Angiotensin II Type 2 Receptor Signaling Attenuates Aortic Aneurysm in Mice Through ERK Antagonism. *Science* 2011;332(6027):361–365.

12. MacFarlane EG et al. Lineage-specific events underlie aortic root aneurysm pathogenesis in Loeys-Dietz syndrome. *J. Clin. Invest.* 2019;129(2):659–675.

13. Chen X et al. Conundrum of angiotensin II and TGF-β interactions in aortic aneurysms. *Curr Opin Pharmacol* 2013;13(2):180–185.

14. Chen X et al. TGF-β Neutralization Enhances AngII-Induced Aortic Rupture and Aneurysm in Both Thoracic and Abdominal Regions. *PLoS ONE* 2016;11(4):e0153811.

15. Wang Y et al. TGF-beta activity protects against inflammatory aortic aneurysm progression and complications in angiotensin II-infused mice. *J. Clin. Invest.* 2010;120(2):422–432.

636 16. Loeys BL et al. Aneurysm syndromes caused by mutations in the TGF-beta receptor. *N.*
637 *Engl. J. Med.* 2006;355(8):788–798.

638 17. Lindsay ME et al. Loss-of-function mutations in TGFB2 cause a syndromic presentation of
639 thoracic aortic aneurysm. *Nature Publishing Group* 2012;44(8):922–927.

640 18. Regalado ES et al. Exome sequencing identifies SMAD3 mutations as a cause of familial
641 thoracic aortic aneurysm and dissection with intracranial and other arterial aneurysms. *Circ. Res.*
642 2011;109(6):680–686.

643 19. Tan CK et al. SMAD3 deficiency promotes inflammatory aortic aneurysms in angiotensin II-
644 infused mice via activation of iNOS. *J Am Heart Assoc* 2013;2(3):e000269.

645 20. Dai X et al. SMAD3 deficiency promotes vessel wall remodeling, collagen fiber
646 reorganization and leukocyte infiltration in an inflammatory abdominal aortic aneurysm mouse
647 model. *Sci Rep* 2015;5(1):10180.

648 21. Doyle AJ et al. Mutations in the TGF-β repressor SKI cause Shprintzen-Goldberg syndrome
649 with aortic aneurysm. *Nature Publishing Group* 2012;44(11):1249–1254.

650 22. Carmignac V et al. In-Frame Mutations in Exon 1 of SKI Cause Dominant Shprintzen-
651 Goldberg Syndrome. *The American Journal of Human Genetics* 2012;91(5):950–957.

652 23. Akiyoshi S et al. c-Ski acts as a transcriptional co-repressor in transforming growth factor-
653 beta signaling through interaction with smads. *J. Biol. Chem.* 1999;274(49):35269–35277.

654 24. Luo K et al. The Ski oncoprotein interacts with the Smad proteins to repress TGFbeta
655 signaling. *Genes & Development* 1999;13(17):2196–2206.

656 25. Stroschein SL et al. Negative feedback regulation of TGF-beta signaling by the SnoN
657 oncoprotein. *Science* 1999;286(5440):771–774.

658 26. Sun Y et al. Interaction of the Ski oncoprotein with Smad3 regulates TGF-beta signaling.
659 *Mol. Cell* 1999;4(4):499–509.

660 27. Xu W et al. Ski acts as a co-repressor with Smad2 and Smad3 to regulate the response to type
661 beta transforming growth factor. *Proc. Natl. Acad. Sci. U.S.A.* 2000;97(11):5924–5929.

662 28. Wu JW et al. Structural mechanism of Smad4 recognition by the nuclear oncoprotein Ski:
663 insights on Ski-mediated repression of TGF-beta signaling. *Cell* 2002;111(3):357–367.

664 29. Liu X et al. Ski/Sno and TGF-beta signaling. *Cytokine Growth Factor Rev.* 2001;12(1):1–8.

665 30. Chen W et al. Competition between Ski and CREB-binding protein for binding to Smad
666 proteins in transforming growth factor-beta signaling. *J. Biol. Chem.* 2007;282(15):11365–
667 11376.

668 31. Gori I et al. Mutations in SKI in Shprintzen-Goldberg syndrome lead to attenuated TGF-β
669 responses through SKI stabilization. *Elife* 2021;10. doi:10.7554/eLife.63545

670 32. Holtwick R et al. Smooth muscle-selective deletion of guanylyl cyclase-A prevents the acute
671 but not chronic effects of ANP on blood pressure. *Proc. Natl. Acad. Sci. U.S.A.*
672 2002;99(10):7142–7147.

673 33. Creyghton MP et al. Histone H3K27ac separates active from poised enhancers and predicts
674 developmental state. *Proc. Natl. Acad. Sci. U.S.A.* 2010;107(50):21931–21936.

675 34. Rada-Iglesias A et al. A unique chromatin signature uncovers early developmental enhancers
676 in humans. *Nature* 2011;470(7333):279–283.

677 35. Visel A et al. ChIP-seq accurately predicts tissue-specific activity of enhancers. *Nature*
678 2009;457(7231):854–858.

679 36. Wang Q et al. Spatial and temporal recruitment of androgen receptor and its coactivators
680 involves chromosomal looping and polymerase tracking. *Mol. Cell* 2005;19(5):631–642.

681 37. Jin Q et al. Distinct roles of GCN5/PCAF-mediated H3K9ac and CBP/p300-mediated
682 H3K18/27ac in nuclear receptor transactivation. *EMBO J.* 2011;30(2):249–262.

683 38. Weinert BT et al. Time-Resolved Analysis Reveals Rapid Dynamics and Broad Scope of the
684 CBP/p300 Acetylome. *Cell* 2018;174(1):231–244.e12.

685 39. Raisner R et al. Enhancer Activity Requires CBP/P300 Bromodomain-Dependent Histone
686 H3K27 Acetylation. *CellReports* 2018;24(7):1722–1729.

687 40. Inoue Y et al. Smad3 is acetylated by p300/CBP to regulate its transactivation activity.
688 *Oncogene* 2007;26(4):500–508.

689 41. Bowers EM et al. Virtual ligand screening of the p300/CBP histone acetyltransferase:
690 identification of a selective small molecule inhibitor. *Chem Biol* 2010;17(5):471–482.

691 42. Kaartinen V, Warburton D. Fibrillin controls TGF-beta activation. *Nat Genet*
692 2003;33(3):331–332.

693 43. Cannaerts E et al. TGF-β signalopathies as a paradigm for translational medicine. *Eur J Med*
694 *Genet* 2015;58(12):695–703.

695 44. Ramirez F et al. Fibrillin microfibrils: multipurpose extracellular networks in organismal
696 physiology. *Physiol Genomics* 2004;19(2):151–154.

697 45. Bertoli-Avella AM et al. Mutations in a TGF-β ligand, TGFB3, cause syndromic aortic
698 aneurysms and dissections. *J. Am. Coll. Cardiol.* 2015;65(13):1324–1336.

699 46. Courtois A et al. A novel SMAD3 mutation caused multiple aneurysms in a patient without
700 osteoarthritis symptoms. *Eur J Med Genet* 2017;60(4):228–231.

701 47. Micha D et al. SMAD2 Mutations Are Associated with Arterial Aneurysms and Dissections.
702 *Hum. Mutat.* 2015;36(12):1145–1149.

703 48. Robinson PN et al. Shprintzen-Goldberg syndrome: fourteen new patients and a clinical
704 analysis. *Am. J. Med. Genet.* 2005;135(3):251–262.

705 49. Zhang B et al. A dynamic H3K27ac signature identifies VEGFA-stimulated endothelial
706 enhancers and requires EP300 activity. *Genome Research* 2013;23(6):917–927.

707 50. Yuan H et al. Involvement of p300/CBP and epigenetic histone acetylation in TGF-β1-
708 mediated gene transcription in mesangial cells. *Am. J. Physiol. Renal Physiol.*
709 2013;304(5):F601–13.

710 51. Petruk S et al. Stepwise histone modifications are mediated by multiple enzymes that rapidly
711 associate with nascent DNA during replication. *Nat Commun* 2013;4:2841.

712 52. Dias JD et al. Methylation of RNA polymerase II non-consensus Lysine residues marks early
713 transcription in mammalian cells. *Elife* 2015;4:387.

714 53. Huang W-S et al. CIL-102-Induced Cell Cycle Arrest and Apoptosis in Colorectal Cancer
715 Cells via Upregulation of p21 and GADD45. *PLoS ONE* 2017;12(1):e0168989.

716 54. Chen G et al. SREBP-1 is a novel mediator of TGFβ1 signaling in mesangial cells. *J Mol*
717 *Cell Biol* 2014;6(6):516–530.

718 55. Santer FR et al. Inhibition of the acetyltransferases p300 and CBP reveals a targetable
719 function for p300 in the survival and invasion pathways of prostate cancer cell lines. *Mol.*
720 *Cancer Ther.* 2011;10(9):1644–1655.

721 56. Marek R et al. Paradoxical enhancement of fear extinction memory and synaptic plasticity by
722 inhibition of the histone acetyltransferase p300. *J. Neurosci.* 2011;31(20):7486–7491.

723 57. Maddox SA et al. p300/CBP histone acetyltransferase activity is required for newly acquired
724 and reactivated fear memories in the lateral amygdala. *Learn. Mem.* 2013;20(2):109–119.

725 58. Su H et al. Histone Acetyltransferase p300 Inhibitor Improves Coronary Flow Reserve in
726 SIRT3 (Sirtuin 3) Knockout Mice. *J Am Heart Assoc* 2020;9(18):e017176.

727 59. Reddy MA et al. Losartan reverses permissive epigenetic changes in renal glomeruli of
728 diabetic db/db mice. *Kidney Int.* 2014;85(2):362–373.

729 60. Hayashi K et al. Renin-angiotensin blockade resets podocyte epigenome through Kruppel-
730 like Factor 4 and attenuates proteinuria. *Kidney Int.* 2015;88(4):745–753.

731 61. Doyle JJ et al. A deleterious gene-by-environment interaction imposed by calcium channel
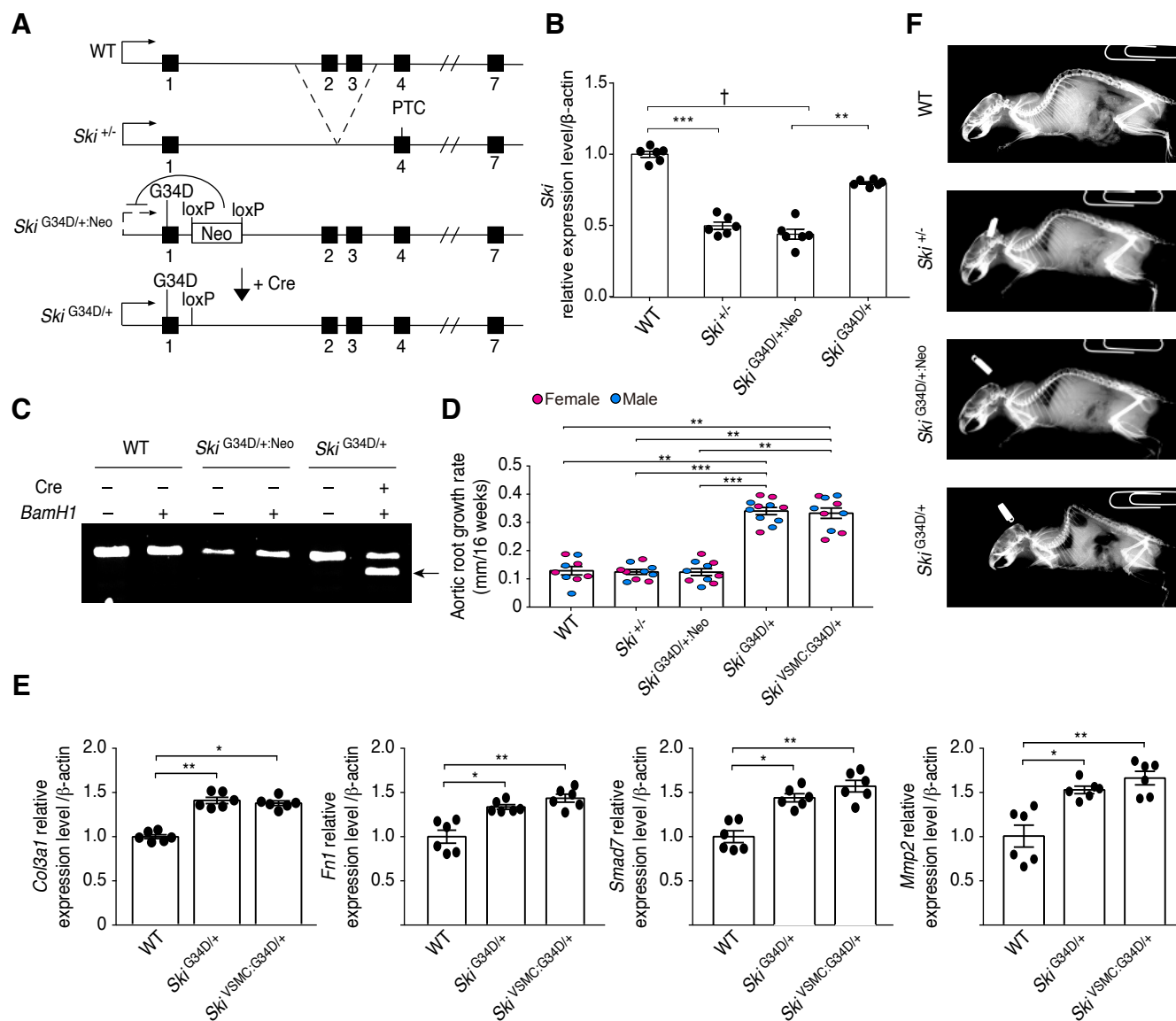732 blockers in Marfan syndrome. *Elife* 2015;4:e81743.

733

Figure 1. Characterization of SGS mouse models. (A) Structure of *Ski* haploinsufficient and *Ski* mutant alleles in mouse models. Deletion of exons 2 and 3 of *Ski* creates a premature termination codon (PTC) in exon 4 of the *Ski* haploinsufficient allele. (B) Mean expression level (±SEM) of *Ski* mRNA in the tail of each mouse line by qPCR. Both *Ski*^{+/-} and *Ski*[G34D/+:Neo] haploinsufficient lines express half the normal complement of *Ski* mRNA, while the *Ski*[G34D/+] mouse line expresses levels comparable to controls; n=6 per group. (C) Expression of WT and mutant *Ski* in each mouse line. The *Ski*[G34D/+] mouse line uniquely expresses the mutant allele, as shown by the BamH1 restriction fragment of amplified cDNA. (D) Mean aortic root growth rate (±SEM) from 8 to 24 weeks of age. Note that *Ski*[G34D/+] and *Ski*[VSMC:G34D/+] mice had significantly greater aortic growth compared to other groups; wild type (n=9), *Ski*^{+/-} (n=10), *Ski*[G34D/+:-Neo] (n=10), *Ski*[G34D/+] (n=11), *Ski*[VSMC:G34D/+] (n=10). (F) Skeletal phenotype: representative spine radiographs for each mouse line at 24 weeks of age. Compared to other mouse lines, only *Ski*[G34D/+] mice demonstrated skeletal deformities. (G) Expression levels of TGFβ target genes (*Col3a1, Fn1, Smad7* and *Mmp2*) relative to β-actin control and normalized to WT expression (±SEM), as determined by qPCR. Compared with WT littermates, *Ski*[G34D/+] mice and *Ski*[VSMC:G34D/+] mice demonstrated increased target gene expression; n=6 for all groups. Non-parametric Kruskal-Wallis test with Dunn's multiple comparison test was used to assess for statistical significance between comparing groups. For all graphs, each bar defines the median with standard error indicated by whiskers and numerical data are presented as scatter dot-plots. *P < 0.05; **P < 0.01; ***P < 0.001; †P < 10⁻⁴.
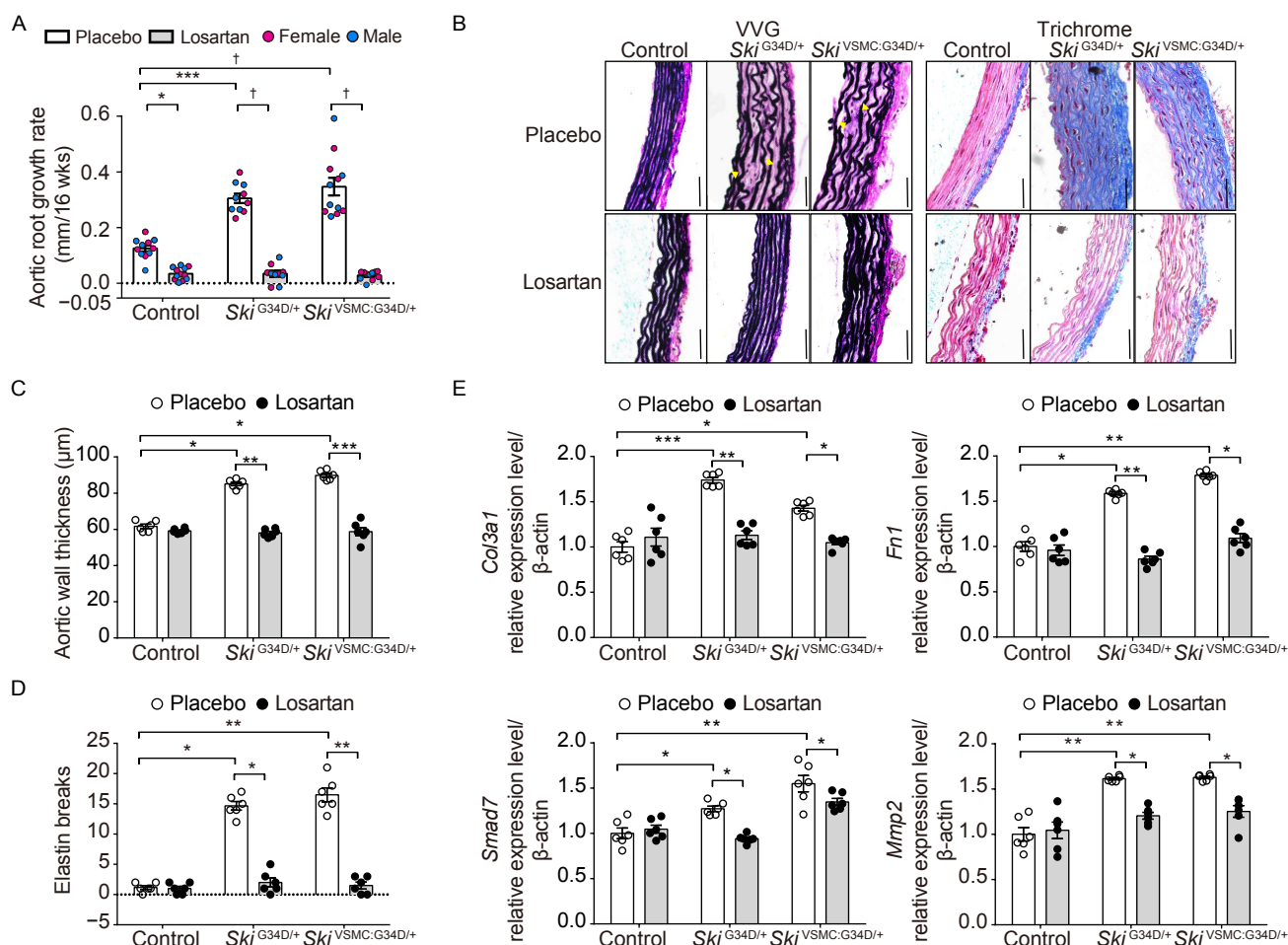
Figure 2. Therapeutic effect of losartan on aortic aneurysm in SGS mice. (A) Mean aortic root growth (±SEM) over 16 weeks of treatment with losartan. Compared with placebo-treated $Ski^{G34D/+}$ and $Ski^{VSMC:G34D/+}$ mice, losartan-treated $Ski^{G34D/+}$ and $Ski^{VSMC:G34D/+}$ mice demonstrated reduced aortic root growth. Control–placebo (n=11), $Ski^{G34D/+}$–placebo (n=10), $Ski^{VSMC:G34D/+}$–placebo (n=12); Control–losartan (n=12), $Ski^{G34D/+}$–losartan (n=10), $Ski^{VSMC:G34D/+}$ mice–losartan (n=11). (B) Representative cross-sections of the aortic root, stained with VVG (left) and Masson's trichrome (right), in placebo- and losartan-treated SGS mice; yellow arrow indicates elastic fiber fragmentation. Black line indicates scale bar (50µm). (C) Aortic wall thickness (±SEM). Compared with controls, placebo-treated $Ski^{G34D/+}$ and $Ski^{VSMC:G34D/+}$ mice demonstrated greater aortic wall thickening, which was significantly reduced in losartan-treated animals; n=6 in all groups. (D) Extent of aortic wall elastic fiber damage, measured by number of elastin breaks (±SEM). Compared with controls, placebo-treated $Ski^{G34D/+}$ and $Ski^{VSMC:G34D/+}$ mice demonstrated increased elastin breaks, which was significantly reduced in losartan-treated animals; n=6 per group. (E) TGFβ target gene expression relative to β-actin and normalized to control expression (±SEM). Compared with controls, $Ski^{G34D/+}$ and $Ski^{VSMC:G34D/+}$ mice demonstrated increased TGFβ target gene expression, which was significantly reduced in losartan-treated animals; n=6 per group. Non-parametric Kruskal-Wallis test with Dunn's multiple comparison test was used to assess for statistical significance between comparing groups. For all graphs, each bar defines the median with standard error indicated by whiskers and numerical data are presented as scatter dot-plots. *P < 0.05; **P < 0.01; ***P < 0.001; †P < 10⁻⁴.
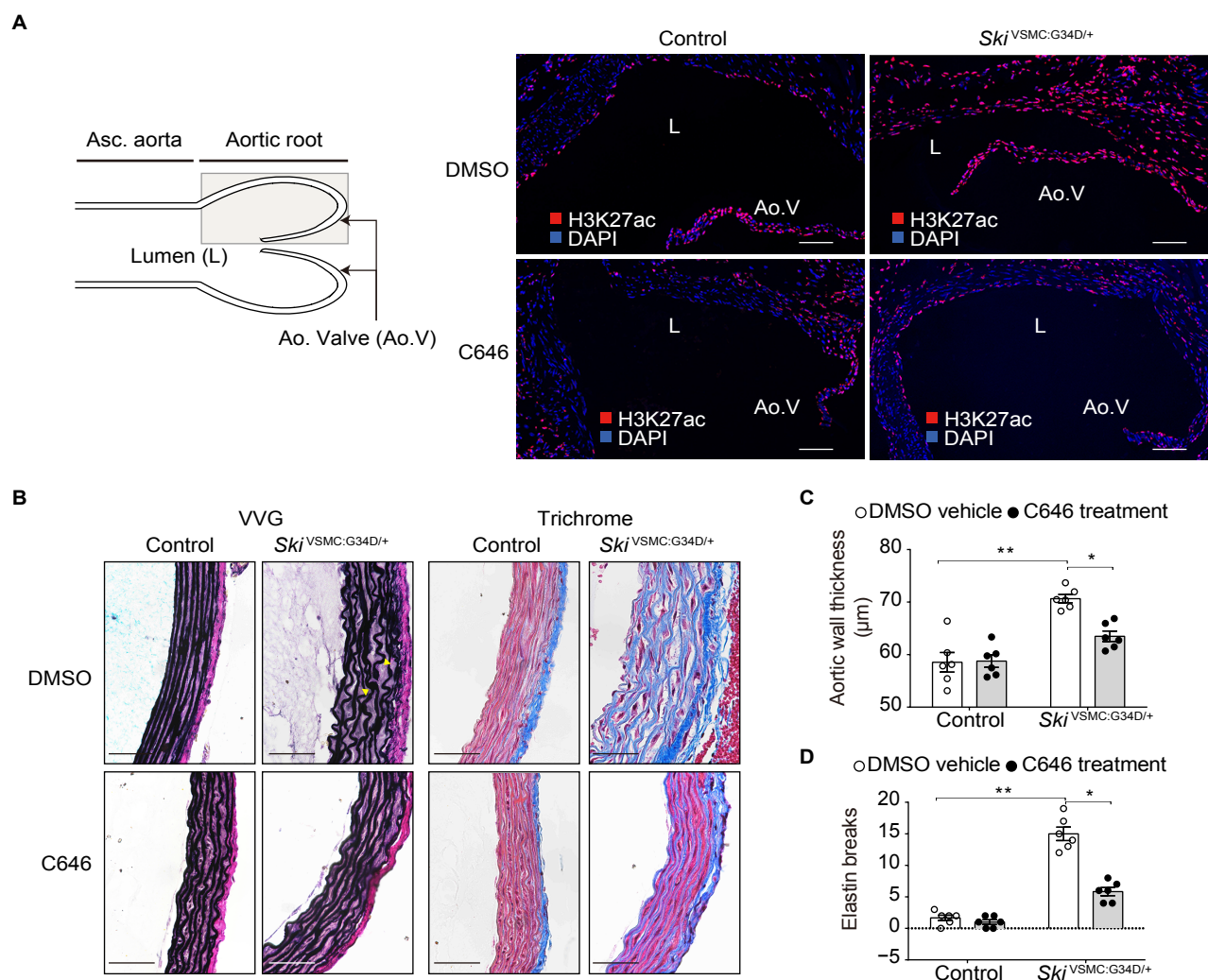
Figure 3. Phenotypic effect of CBP/P300 inhibition using C646 on aortic root aneurysm in mouse models of SGS. (A) Representative immunofluorescence image of aortic root samples of control and $Ski^{VSMC:G34D/+}$ mice treated with either C646 or vehicle (DMSO) probed for histone 3 lysine 27 acetylation (H3K27ac). Compared with controls, $Ski^{VSMC:G34D/+}$ mice demonstrated increased acetylation, which was reduced by C646 treatment. White line indicates scale bar (50μm). (B) Aortic root histology in DMSO- and C646-treated control and $Ski^{VSMC:G34D/+}$ mice. Images show representative cross-sections stained with VVG (left) and Masson's trichrome stain (right). Yellow arrows indicate elastic fiber breaks. Black line indicates scale bar (50μm). (C) Aortic wall thickness (±SEM) in DMSO- and C646-treated control and SGS mice. Compared with controls, DMSO-treated $Ski^{VSMC:G34D/+}$ animals showed greater medial wall thickening, which was reduced in C646-treated $Ski^{VSMC:G34D/+}$ littermates; n=6 for all groups. (D) Mean number of elastin breaks (±SEM) in DMSO- and C646-treated control and SGS mice. Compared with controls, DMSO-treated $Ski^{VSMC:G34D/+}$ mice showed more elastin breaks, which was prevented by C646 treatment; n=6 for all groups. Non-parametric Kruskal-Wallis test with Dunn's multiple comparison test was used to assess for statistical significance between comparing groups. For all graphs, each bar defines the median with standard error indicated by whiskers and numerical data are presented as scatter dot-plots. *P < 0.05; **P < 0.01.
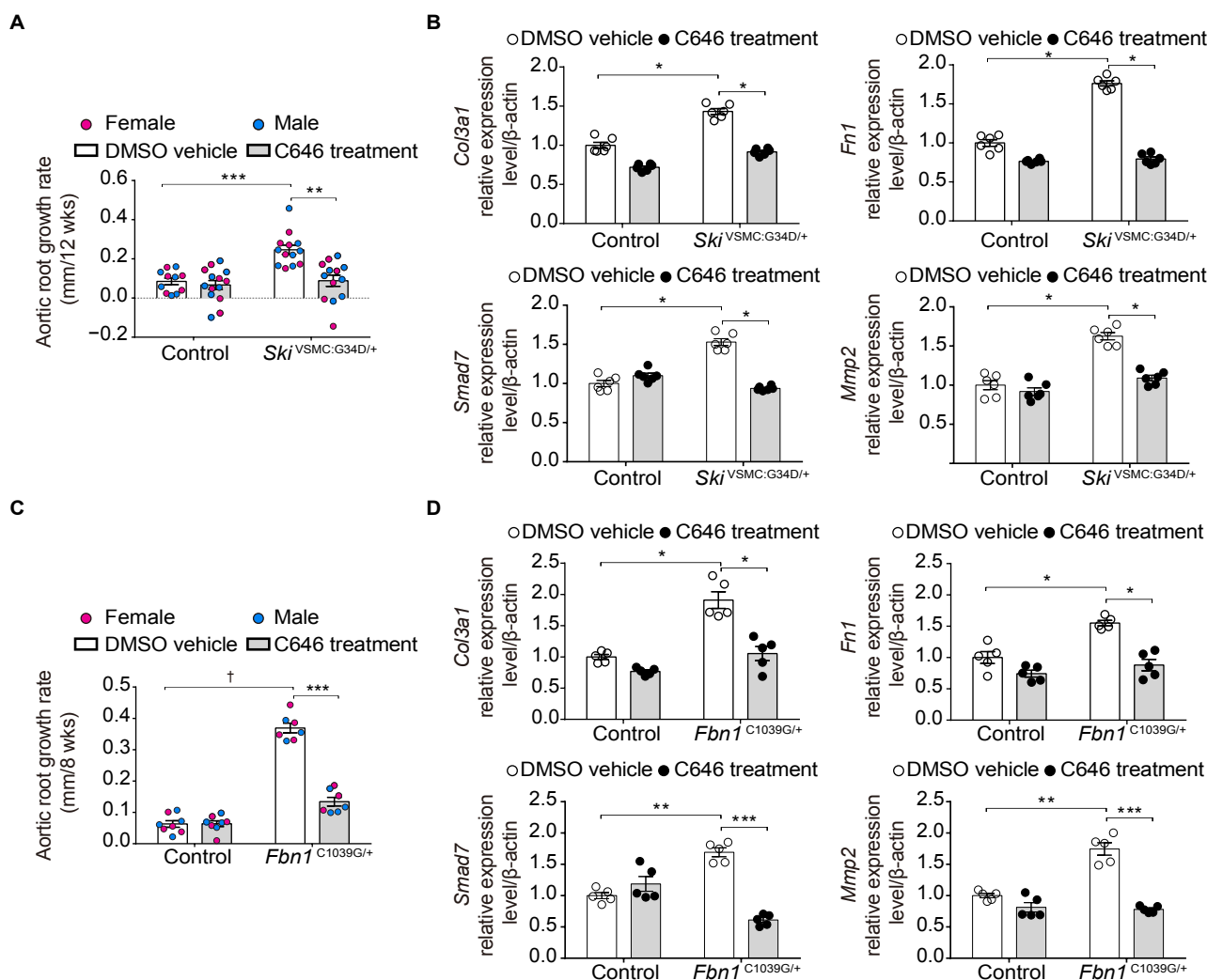
Figure 4. Therapeutic effect of CBP/P300 inhibition using C646 on aortic root aneurysm in mouse models of SGS and MFS. (A) Mean aortic root growth over 12 weeks of treatment with C646 in control and *Ski*VSMC:G34D/+ mice. Compared with controls, *Ski*VSMC:G34D/+ mice demonstrated significantly greater aortic root growth, which was reduced by treatment with C646; Control–DMSO (n=11), *Ski*VSMC:G34D/+–DMSO (n=13); Control–C646 (n=14), *Ski*VSMC:G34D/+–C646 (n=13). (B) TGFβ target gene expression relative to β-actin and normalized to control expression (±SEM), as determined by qPCR. Compared with controls, *Ski*VSMC:G34D/+ mice showed increased target gene expression, which was reduced by C646 treatment; n=6 per group. (C) Mean aortic root growth over 8 weeks of treatment with C646 in control and MFS (*Fbn1*C103934G/+) mice. Compared with DMSO-treated MFS mice, C646-treated MFS animals had a significant reduction in aortic root growth rate; Control–DMSO (n=8), MFS–DMSO (n=8); Control–C646 (n=7), MFS–C646 (n=7). (D) TGFβ target gene expression relative to β-actin and normalized to control expression (±SEM), as determined by qPCR. Compared with controls, MFS (*Fbn1*C103934G/+) mice had significantly increased target gene expression, which was reduced in C646-treated MFS animals. Non-parametric Kruskal-Wallis test with Dunn's multiple comparison test was used to assess for statistical significance between comparing groups. For all graphs, each bar defines the median with standard error indicated by whiskers and numerical data are presented as scatter dot-plots. *P < 0.05; **P < 0.01; ***P < 0.001; †P < 10^{-4}.